

# Intrinsic Integration<sup>\*</sup>

Navdeep Dahiya<sup>a</sup>, Martin Mueller<sup>b</sup>, Anthony Yezzi<sup>a,\*</sup>

<sup>a</sup>*Electrical & Computer Engineering, Georgia Institute of Technology, Atlanta, GA, USA*

<sup>b</sup>*Rivian Automotive, Palo Alto, CA, USA*

---

## Abstract

If we wish to integrate a function  $h|\Omega \subset \mathbb{R}^n \rightarrow \mathbb{R}$  along a single  $T$ -level surface of a function  $\psi|\Omega \subset \mathbb{R}^n \rightarrow \mathbb{R}$ , then a number of different methods for extracting finite elements appropriate to the dimension of the level surface may be employed to obtain an explicit representation over which the integration may be performed using standard numerical quadrature techniques along each element. However, when the goal is to compute an entire continuous family  $m(T)$  of integrals over all the  $T$ -level surfaces of  $\psi$ , then this method of explicit level set extraction is no longer practical. We introduce a novel method to perform this type of numerical integration efficiently by making use of the coarea formula. We present the technique for discretization of the coarea formula and present the algorithms to compute the integrals over families of  $T$ -level surfaces. While validation of our method in the special case of a single level surface demonstrates accuracies close to more explicit isosurface integration methods, we show a sizable boost in computational efficiency in the case of multiple  $T$ -level surfaces, where our coupled integration algorithms significantly outperform sequential one-at-a-time application of explicit methods.

*Keywords:* numerical integration, level set methods, coarea formula, implicit surfaces, quadrature

*2010 MSC:* 65D30, 65D18, 65D19

---

## 1. Introduction

Level set methods for capturing moving fronts introduced by Osher and Sethian [1] have proven to be a robust numerical device for large collection of diverse problems. These methods are frequently used for propagating interfaces in computational physics [2, 3] and fluid dynamics [4], constrained optimization [5, 6], and computer vision [7, 8] among others. Consequently, the problem of numerical integration of a function over volumes and surfaces implicitly defined by a fixed iso-contour/surface of a level set function frequently arises. Over the years many different approaches and methods have been developed for these types of numerical integration problems.

The traditional approach for evaluating such integrals has been to make use of the regularized Dirac delta or the Heaviside function [1]. In [9], the authors showed the standard regularization approaches to be inconsistent and that they may lead to non convergent solutions with  $O(1)$  errors. Enquist et al. [10] later presented discretization techniques for the Dirac delta that were first order accurate with a second order convergence rate. In [11], Smereka further developed a second order accurate discretization of the Dirac delta function with application to calculating line and surface integrals in level set based methods.

Another class of methods explicitly reconstruct the interface to find a faceted mesh representation of the surface through various methods like marching cubes [12] or marching tetrahedra [13, 14] and then

---

<sup>\*</sup>This work was funded by the National Institutes of Health under grant no. R01-HL-143350 and Army Research Office under grant no. W911NF-18-1-0281.

<sup>\*</sup>Corresponding author

*Email addresses:* ndahiya3@gatech.edu (Navdeep Dahiya), martin.mueller@gatech.edu (Martin Mueller), ayezzi@ece.gatech.edu (Anthony Yezzi)

apply standard quadrature schemes to the surface and volume elements. In [15], Min and Gibou presented a geometric technique for calculating such integrals involving discretizing the interface into simplices and using numerical integration quadrature rules on the simplices. They showed the approach to be second-order accurate and being robust to interface perturbation on the grid. They showed several practical examples and compared their results to the techniques introduced by Smereka in [11].

In yet another approach making use of the well known divergence theorem, Müller et al. [16] presented a simple tree based approach and showed it to be comparable to the methods of Min-Gibou and Smereka in accuracy and convergence. In [17] Müller et al. presented a new method based on the solution of a small linear system based on a simplified variant of moment-fitting equations. The authors showed the method to be several orders of magnitude more accurate than earlier approaches. More recently, [18] presented a high-order accurate numerical quadrature method for evaluating integrals over curved surfaces and volumes defined via a fixed isosurface of a function restricted to a given hyperrectangle. The method converts the implicitly defined geometry into the graph of a height function leading to a recursive algorithm on the number of dimensions requiring one-dimensional root finding and one-dimensional Gaussian quadrature.

In [19], the authors proposed a formulation for computing integrals of the form,  $\int_{\partial\Omega} v(\mathbf{x}(s)) ds$  in the levelset framework, when the domain  $\Omega$  is represented implicitly by the signed distance function to its boundary  $\partial\Omega$ . The authors expressed this integral as an average of integrals over nearby level sets of  $d_{\partial\Omega}$ , where these nearby level sets continuously sweep a thin tubular neighborhood around the boundary  $\partial\Omega$  of radius  $\epsilon$ . With this formulation, the authors proposed a numerical method based on integral equation formulations for solving the Poisson problem with constant coefficients, subject to Dirichlet, Neumann, Robin or mixed boundary conditions. This proposed formulation involved an exact formulation for computing boundary integrals in the level set framework, and provided a natural way of defining and computing boundary integrals in applications using the closest point formulations [20, 21]. In [22], the authors further extended this technique to include integration along curves in three dimensions. Here the authors proposed a new formulation using the closest point mapping for integrating over smooth curves and surfaces with boundaries that are described by their closest point mappings. The authors studied various aspects of this formulation and provided a geometric interpretation in terms of the singular values of the Jacobian matrix of the closest point mapping. In [23], the authors further extended the framework of [19, 22], and proposed an extrapolative approach for computing integrals over a class of piecewise smooth hypersurfaces, given implicitly via a level set function. Although this method was based on the classical approximation used in the level set framework that smears out the Dirac  $\delta$ -function to a bump function with a compact support, in this work the authors combined the classical formulas for the more challenging cases in which the hypersurfaces have kinks and corners. The authors made use of special kernels with vanishing moments for the approximation of the Dirac  $\delta$ -function, and their proposed method did not require any local explicit parameterization of the hypersurface, nor the explicit locations of the corners and kinks on the hypersurface.

As we have seen so far that if we wish to integrate a function  $h|\Omega \subset \mathbb{R}^n \rightarrow \mathbb{R}$  along a single  $T$ -level surface of a function  $\psi$ , then a number of different methods for extracting finite elements appropriate to the dimension of the level surface (line segments, triangles, tetrahedra, etc.) may be employed to obtain an explicit representation over which the integration may be performed using standard numerical quadrature techniques along each element. However, when the goal is to compute the an entire continuous family  $m(T)$  of integrals over all the  $T$ -level surfaces of  $\psi$ ,

$$m(T) = \int_{\psi^{-1}(T)} h ds$$

then this method of explicit level set extraction is no longer practical. An alternative is to first construct the anti-derivative  $M(T)$

$$M(T) = \int_{-\infty}^T \int_{\psi^{-1}(\tau)} h ds d\tau = \int_{\psi(x) < T} h \|\nabla \psi\| dx$$

which, by the coarea formula, is obtained by volumetric integration of  $h\|\nabla \psi\|$  over the progressively expanding volume where  $\psi(x) < T$  (the  $T$ -sublevel set of  $\psi$ ), and then differentiate the result to obtain  $m(T) = M'(T)$ .

In this paper we present the discretization of this coarea formula, derive the expressions for calculation the partial volumes across grid cells and present an algorithm for efficiently computing  $M(T)$ . We also present an even more efficient algorithm for the case where the level set function is a signed distance function. By effectively coupling the computation of the integrals over whole range of different isosurfaces, our methods lead to efficient computation of the entire family of integrals. However, it is still instructive to compare the accuracy of our methods by computing the integral for a single level surface and comparing the results to traditional single isosurface methods. Accordingly, we present results showing comparable accuracy with the methods developed in Min-Gibou [15]. Additionally and more importantly, we can use a brute force approach of employing traditional single isosurface integration methods sequentially, one at a time, to each level surface contained in a range and compare the resulting integrals to our approach of computing the whole range of integrals in a coupled manner. We present experiments illustrating the significant computational efficiency afforded by our coupled integration methods over such a brute force approach required by traditional single isosurface methods.

The paper is organized as follows. Our main derivations and algorithms are in 2, experimental results are in 3, and the conclusions follow in 4.

## 2. Numerical Integration along Level Sets

Our goal is to compute the entire continuous family of integrals  $m(T)$  of a general function  $h|\Omega \subset \mathbb{R}^n \rightarrow \mathbb{R}$  over all the  $T$ -level surfaces of  $\psi$ ,

$$m(T) = \int_{\psi^{-1}(T)} h \, ds$$

In order to avoid the inefficient explicit extraction of the  $T$ -level surfaces of  $\psi$ , we first construct the anti-derivative  $M(T)$

$$M(T) = \int_{-\infty}^T \int_{\psi^{-1}(\tau)} h \, ds \, d\tau = \int_{\psi(x) < T} h \|\nabla \psi\| \, dx$$

which, by the coarea formula, is obtained by volumetric integration of  $h\|\nabla \psi\|$  over the progressively expanding volume where  $\psi(x) < T$  (the  $T$ -sublevel set of  $\psi$ ), and then differentiate the result to obtain  $m(T) = M'(T)$ .

### 2.1. Discretization

We will assume that the functions  $h$  and  $\psi$  are both sampled over matching Cartesian grids with sample locations denoted by  $x_i \in \mathbb{R}^n$  and with uniform spatial increments, represented by the constant  $n$ -dimensional *space step vector*  $\Delta x$ , between samples along each orthogonal direction<sup>1</sup>. Associated to each *grid point*  $x_i$  will be the corresponding *grid cell*, denoted by  $\text{cell}(\Delta x, x_i)$ , which refers to the  $n$ -dimensional rectangle centered around the grid point  $x_i$  and with edge lengths in orthogonal directions matching the elements of the space step vector  $\Delta x$ . Finally, we will also need to choose a *range interval*  $[T_{\min}, T_{\max}]$  as well as a constant *range increment*  $\Delta T$  for our discretized representation of the continuous functions  $M$  and  $m$ . Note that, unlike the space step vector  $\Delta x$ , the range increment  $\Delta T$  is a scalar constant.

### 2.2. Cell-wise linear approximation

We assume that, in addition to the available sample  $\psi(x_i)$  of the level set function  $\psi$  at each grid point  $x_i$ , we have (or can compute) an estimate of the gradient  $\nabla \psi(x_i)$  at each grid point as well. We may then construct a linear approximation  $\psi_i$  of the level set function within each cell  $\text{cell}(\Delta x, x_i)$  that matches  $\psi$  and its first order derivatives at the grid point  $x_i$  in the center of the cell.

$$\psi_i(x) = \psi(x_i) + (x - x_i) \cdot \nabla \psi(x_i), \quad x \in \text{cell}(\Delta x, x_i)$$

---

<sup>1</sup>The overloaded use of  $\Delta$  to represent a either a discrete interval size or the Lapacian operator is disambiguated by the type of symbol it precedes (a variable or measurement versus a function).

The minimum and maximum values of  $\psi_i$  are attained at opposite vertices of its corresponding cell and easily shown to be

$$\begin{aligned}\min \psi_i &= \psi(x_i) - \frac{\|\Delta x \odot \nabla \psi(x_i)\|_1}{2} \\ &= \psi(x_i) - \frac{\Delta x}{2} \cdot (\nabla \psi(x_i) \odot \text{sgn} \nabla \psi(x_i)) \\ \max \psi_i &= \psi(x_i) + \frac{\|\Delta x \odot \nabla \psi(x_i)\|_1}{2} \\ &= \psi(x_i) + \frac{\Delta x}{2} \cdot (\nabla \psi(x_i) \odot \text{sgn} \nabla \psi(x_i))\end{aligned}$$

where  $\|\bullet\|_1$  denotes the  $L^1$  vector norm (sum of the absolute values of the elements), where  $\odot$  denotes the Hadamard product (element-wise multiplication), and where we have generalized the signum function  $\text{sgn}(\bullet)$  to act on a vector of real numbers by simple element-wise application of the standard signum function (which maps positive numbers to 1, negative numbers to -1, and 0 to 0). Cell locations (along the boundary if  $\nabla \psi(x_i) \neq 0$ ) where these extrema are attained can be calculated using the following formulas

$$\begin{aligned}\arg \min \psi_i(x) &= x_i - \frac{\Delta x \odot \text{sgn} \nabla \psi(x_i)}{2} \\ \arg \max \psi_i(x) &= x_i + \frac{\Delta x \odot \text{sgn} \nabla \psi(x_i)}{2}\end{aligned}$$

which yield opposite vertices of the cell if and only if these extrema are attained at unique locations. If one or more of the elements of  $\text{sgn} \nabla \psi(x_i)$  are zero (due to the corresponding element of  $\nabla \psi(x_i)$  being zero), then the minimum, as well as the maximum, will be attained at multiple cell boundary locations (including non-vertex points) rather than just at one unique vertex. In such cases, multiple pairs of opposite vertices will exhibit the same extremal values of  $\psi_i$  within the cell, but the formulas above will not yield any such pair. Such extremal vertex pair combinations can be obtained, however, by substituting all of the zero-elements of  $\text{sgn} \nabla \psi(x_i)$  in the formulas for  $\arg \min \psi_i$  and  $\arg \max \psi_i$  above with any combination of  $\pm 1$  (each combination will yield a different pair of opposite min/max vertices so long as at least one of original elements was non-zero to begin with). If only one such vertex pair is needed, then a simple and systematic method for obtaining one would be to replace the vector element-wise signum function in the previous formulas with a vector element-wise sign function

$$S_i = \text{sign} \nabla \psi(x_i)$$

which produces a binary valued output vector  $S_i$  whose elements are either -1 (for negative input elements) or 1 otherwise (for non-negative input elements). Using this convention, we always obtain unique set of opposite extremal vertices  $v_{\min,i}$  and  $v_{\max,i}$  via the following formulas.

$$\begin{aligned}v_{\min,i} &= x_i - \frac{\Delta x \odot S_i}{2} \\ v_{\max,i} &= x_i + \frac{\Delta x \odot S_i}{2}\end{aligned}$$

We will refer to this unique choice of opposite extremal vertices as the *minimal vertex* and the *maximal vertex*, respectively, of the cell centered around grid point  $x_i$ .

Finally, note that moving from the minimal to the maximal vertex requires a combination of displacements along each orthogonal grid direction with distances given by the corresponding grid step sizes stored in the vector  $\Delta x$ . Since  $\psi_i$  changes linearly, its total increase as we move from  $v_{\min,i}$  to  $v_{\max,i}$  can likewise be decomposed as a combination of *directional increases* across the cell along each of these orthogonal grid directions, which we represent by the vector  $D_i$

$$\underbrace{D_i}_{\text{increases}} = \underbrace{\Delta x}_{\text{distances}} \odot \underbrace{S_i \odot \nabla \psi(x_i)}_{\text{rates of increase}}$$

The sum of these directional increases yields the total cell increase which can be expressed in several ways:

$$\text{total cell increase} = \max \psi_i - \min \psi_i = \|D_i\|_1 = \|\Delta x \odot \nabla \psi(x_i)\|_1 = (S_i \odot \Delta x) \cdot \nabla \psi(x_i)$$

### 2.3. Cell coordinates

Let us introduce local cell coordinates<sup>2</sup>  $z = (z_1, \dots, z_n)$  which represent a shifted, scaled, and mirrored version of the global spatial coordinates  $x$ , such that a given grid cell,  $\text{cell}(\Delta x, x_i)$ , may be locally parameterized by the unit  $n$ -dimensional cube with minimal vertex at the origin  $z = (0, \dots, 0)$  and the maximal vertex at  $z = (1, \dots, 1)$ . The resulting change of coordinates is expressed by the following formulas (where we use the symbol  $\odot$  to denote vector element-wise division or, stated more technically, multiplication by the Hadamard inverse of the right-hand operand).

$$x = v_{\min,i} + (\Delta x \odot S_i) \odot z \quad \text{or} \quad z = (x - v_{\min,i}) \odot (\Delta x \odot S_i)$$

Note that  $v_{\min,i}$  constitutes the translation,  $\Delta x$  the rescaling, and  $S_i$  the reflection. The Jacobian and its determinant for this change of coordinates are given as follows

$$\frac{dx}{dz} = \text{diag}(\Delta x \odot S_i), \quad \det \left( \frac{dx}{dz} \right) = \pm \prod \Delta x$$

where  $\text{diag}(\bullet)$  denotes the diagonal  $n \times n$  matrix whose diagonal entries match the elements of the  $n$ -dimensional input vector, and where, using a slight abuse of notation, we have written  $\prod \Delta x$  to denote the product of the elements of the vector  $\Delta x$  of grid space steps. Note that the sign of the determinant will be negative if there is an odd number of -1 entries in the gradient sign vector  $S_i$ , otherwise the sign will be positive. The sign is irrelevant, though, when utilizing this change of variables in the context of integration, where only the absolute value of the determinant is needed.

$$dx = \left( \prod \Delta x \right) dz$$

Finally, when changing variables from  $x$  to  $z$  we will find the following relation useful.

$$\begin{aligned} \psi_i(x) &= \psi_i(v_{\min,i} + (\Delta x \odot S_i) \odot z) \\ &= \psi(x_i) + (v_{\min,i} - x_i) \cdot \nabla \psi(x_i) + (\Delta x \odot S_i \odot z) \cdot \nabla \psi(x_i) \\ &= \psi(x_i) - \frac{\Delta x}{2} \cdot (S_i \odot \nabla \psi(x_i)) + (\Delta x \odot S_i \odot z) \cdot \nabla \psi(x_i) \\ &= \min \psi_i + (\Delta x \odot S_i \odot z) \cdot \nabla \psi(x_i) \\ &= \min \psi_i + z \cdot (\Delta x \odot S_i \odot \nabla \psi(x_i)) \\ &= \min \psi_i + z \cdot D_i \end{aligned}$$

### 2.4. Partial volumes

Our volumetric integration of  $h\|\nabla \psi\|$  over the progressively expanding  $T$ -sublevel set  $\psi(x) < T$  will be carried out numerically via cell-wise addition by approximating  $h\|\nabla \psi\|$  as constant over each grid cell  $x_i$  and then multiplying this by the estimated volume of the cell subset where  $\psi(x) < T$ . We will refer to volume within the cell of this  $T$ -sublevel set as the *partial volume* of the cell, denoted by  $V_i(T)$  to reflect

---

<sup>2</sup>Notice that a subscript on the cell coordinate symbol  $z$  refers to one of its vector components rather than one of the enumerated grid points as for subscripts on other symbols such as  $x$ ,  $S$ , and  $\psi$ . Thus  $z_k$  denotes the  $k$ 'th element of  $z$ , whereas  $x_i$  denotes the location of the grid point indexed by  $i$ , just as  $\psi_i$  denotes the linear approximation of  $\psi$  over the corresponding grid cell indexed by  $i$ . Since the cell coordinates are local, and therefore depend upon a already-specified choice of grid cell, there is no need to continue representing the grid point index in the coordinate's notation, and so we exploit the use of subscripts for this other purpose here. To reinforce this difference in subscript meaning and reduce any resulting confusion, we reserve the use of the subscript symbol  $i$  exclusively in reference to a grid point and utilize a different subscript symbol (such as  $k$ ) whenever indicating a vector component.

its dependence on the level set value  $T$ . We will consider all of the cell to belong to this  $T$ -sublevel set if  $\max \psi_i \leq T$  (thereby setting  $V_i(T)$  to full cell volume  $\prod \Delta x$ ); we will consider a cell to be fully excluded if  $\min \psi_i \geq T$  (thereby setting  $V_i(T)$  to zero); and we will consider a cell to be partially included and partially excluded whenever  $\min \psi_i < T < \max \psi_i$ . Consistent with our convention to determine fully included and fully excluded cells, we will use the same linear approximation  $\psi_i$  within each cell to calculate  $V_i(T)$  for partially included and partially excluded cells as follows.

$$\begin{aligned}
V_i(T) &= \int_{\text{cell}(\Delta x, x_i)} H(T - \psi_i(x)) dx \quad (\text{where } H \text{ denotes the Heaviside function}) \\
&= \int_{\text{cell}(\Delta x, x_i)} H\left(\frac{T - \psi_i(x)}{\|D_i\|_1}\right) dx \\
&= \left(\prod \Delta x\right) \underbrace{\int_0^1 \cdots \int_0^1 H\left(\frac{T - \min \psi_i - z \cdot D_i}{\|D_i\|_1}\right) dz_1 \cdots dz_n}_v \\
&= \left(\prod \Delta x\right) \int_0^1 \cdots \int_0^1 H\left(\frac{T - \min \psi_i}{\max \psi_i - \min \psi_i} - z \cdot \frac{D_i}{\|D_i\|_1}\right) dz_1 \cdots dz_n \\
&= \left(\prod \Delta x\right) v\left(\underbrace{\frac{T - \min \psi_i}{\max \psi_i - \min \psi_i}}_{\tau}, \underbrace{\frac{D_i}{\|D_i\|_1}}_d\right)
\end{aligned}$$

In this last line, we have defined the function  $v$  which represents the *fractional volume* of the unit cube given the *fractional total increase*  $\tau$  associated with the level set value  $\tau$  and the vector  $d$  of *fractional directional increases* across the cell. The partial volume  $V_i$  is then obtained by multiplying the total cell volume  $\prod \Delta x$  by the fractional volume  $v$

$$v(\tau, d) = \int_0^1 \cdots \int_0^1 H(\tau - z \cdot d) dz_1 \cdots dz_n$$

Notice that if  $\min \psi_i < T < \max \psi_i$  then  $0 < \tau < 1$ . Moreover, since the coefficients of  $D_i$  are all non-negative, its  $L^1$ -norm is given by the sum of its elements (the increases in  $\psi_i$  across the cell along each orthogonal direction), meaning that the elements  $d_1, \dots, d_n$  of the  $L^1$ -normalized vector of *fractional directional increases* across the cell will sum to 1. In deriving dimension-specific formulas for  $v$ , it is helpful to assume, without loss of generality (since the order of integration with respect to the cell coordinates  $z_1, \dots, z_n$  can be permuted without consequence and since each cell coordinate ranges across the same unit interval) that  $d_1, \dots, d_n$  are sorted in increasing order and therefore  $d_1 \leq d_2 \leq \cdots \leq d_n$ . When implementing the resulting formulas, however, it will be important to sort the actual elements of  $d$  accordingly before applying such formulas.

#### 2.4.1. 2D fractional volume (area) formulas

Here we derive the fractional volume formula for  $v$  in the 2D case (and refer to it, accordingly, as the fractional area). There are three different geometries to consider in the 2D case, which are illustrated in 1 where the lower-left corner represents the origin of the unit square, with cell coordinates (0,0) and where the upper right corner has cell coordinates (1,1). The horizontal axis is associated with cell coordinate  $z_1$ , which means that  $v(1,0)=d_1$ , while the vertical axis is associated with cell coordinate  $z_2$ , which means that  $v(0,1)=d_2$ . In the case that  $0 < \tau < d_1$ , the fractional area  $v(\tau, d)$  is represented in the left image of 1 by the lower-left triangle with base width  $\frac{\tau}{d_1}$  and height  $\frac{\tau}{d_2}$ . As  $\tau$  increases and eventually falls within the range  $d_1 < \tau < d_2$ , the fractional area  $v$  is represented in the middle image of 1 by a trapezoid with base width 1, left height  $\frac{\tau}{d_2}$  and right height  $\frac{\tau - d_1}{d_2}$ . Finally as  $\tau$  increases further to fall within the final range  $d_2 < \tau < 1$ , the fractional area  $v$  is represented in the right image of 1 by the complement of the upper-right triangle with base width  $\frac{1 - \tau}{d_1}$  and height  $\frac{1 - \tau}{d_2}$ . Thus, using the standard geometric area formulas for the triangle and

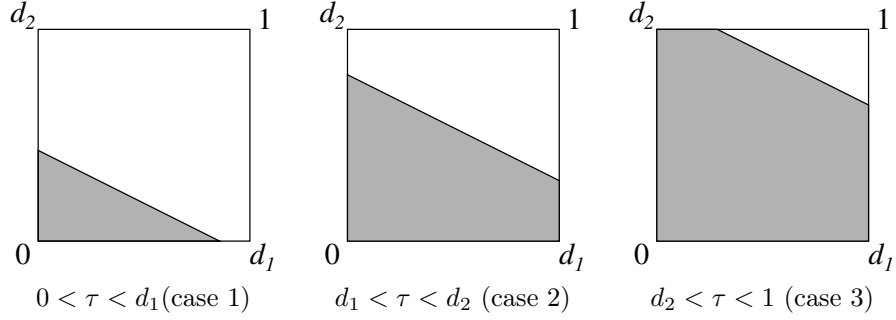


Figure 1: Different possible fractional 2D cell geometries

trapezoid and further noting that the  $L^1$ -normalization of  $d$  means that  $d_2=1-d_1$ , it is easy to derive the following fractional area formulas in 2D.

$$v_{2D}(\tau, d) = \begin{cases} \frac{1}{2} \frac{\tau^2}{d_1 d_2}, & [1] \quad 0 \leq \tau < d_1 \\ \frac{1}{2} + \frac{\tau - \frac{1}{2}}{d_2} = \frac{\tau - \frac{d_1}{2}}{d_2}, & [2] \quad d_1 \leq \tau \leq 1 - d_1 \\ \frac{\tau - \frac{1}{2} d_1}{d_2} \\ 1 - \frac{1}{2} \frac{(1-\tau)^2}{d_1 d_2}, & [3] \quad 1 - d_1 < \tau \leq 1 \end{cases}$$

In the special case where the  $\nabla\psi(x_i)$  is parallel to one of the Cartesian grid axes, this will mean, by our ordering assumption, that  $d_1=0$  and  $d_2=1$  and therefore only the middle case will apply, with the simplified formula of  $v_{2D}(\tau, d) = \tau$ . This simple expression may also be interpreted as the “fractional length”  $v_{1D}(\tau)$  of a 1D cell which is simply identical to the total fractional increase  $\tau$ .

$$v_{2D}\left(\tau, \begin{bmatrix} d_1=0 \\ d_2 \end{bmatrix}\right) = v_{1D}(\tau) = \tau$$

#### 2.4.2. General fractional volume formulas

While it is convenient in 2D, due to the simplicity and limited number of geometries, to directly derive the fractional area formulas based on the custom geometries associated to each of the three separate cases, such an approach becomes considerably more complicated in three dimensions, and completely impractical in even higher dimensions. A more systematic method is to start by noting that for  $0 < \tau < d_1$  the fractional partial volume corresponds to an  $n$ -dimensional simplex whose vertices consist of an orthogonal corner at the cell origin  $(0, \dots, 0)$  together with the intersections of a hyperplane with each of the orthogonal cell coordinate axes. Since each of these axis intersections occur within the unit interval of the associated cell coordinate (by our assumption that  $0 < \tau < d_1$  together with our ordering assumption  $d_1 \leq \dots \leq d_n$ ), the resulting simplex is fully contained within the cell and therefore its volume can be equated with the fractional volume  $v(\tau, d)$ . Noting that the simplex intersects the  $k$ 'th axis at coordinate value  $z_k = \frac{\tau}{d_k}$  (by solving  $\tau - z \cdot d = 0$  when all the other cell coordinates are set to zero), the simplex volume  $v_{(0, \dots, 0)}(\tau, d)$  may be expressed as follows.

$$v_{(0, \dots, 0)}(\tau, d) = \frac{1}{n!} \prod_{k=1}^n \frac{\tau}{d_k} = \frac{\tau^n}{n! \prod d}$$

As  $\tau$  increases to enter the next range interval  $d_1 < \tau < d_2$  this simplex volume will exceed the fractional cell volume since part of this simplex falls outside of the unit cell (the portion crossing the  $z_1=1$  hyperplane). However, the portion of this simplex which falls outside of the cell is another simplex within the  $z_1 > 0$  half-space with an orthogonal corner at  $(1, 0, \dots)$  whose edge length along each orthogonal  $z_k$  axis is given

by  $\frac{\tau-d_1}{d_k}$ . As such, its volume is easily expressed as well by

$$v_{(1,0,\dots)}(\tau, d) = \frac{1}{n!} \prod_{k=1}^n \frac{\tau - d_1}{d_k} = \frac{(\tau - d_1)^n}{n! \prod d}$$

allowing us to express the fractional cell volume  $v(\tau, d)$  as the difference between the full simplex volume  $v_{(0,\dots,0)}(\tau, d)$  and this *spillover simplex volume*  $v_{(1,0,\dots)}(\tau, d)$ . As  $\tau$  further increases to fall within the interval  $d_2 < \tau < d_3$  then additional spillover occurs within the half-space  $z_2 > 1$  hyperplane, which also takes the form of a simplex with an orthogonal corner at  $(0,1,0,\dots)$  with edge lengths given by  $\frac{\tau-d_2}{d_k}$  along each  $z_k$  axis and whose volume can therefore be expressed as follows.

$$v_{(0,1,0,\dots)}(\tau, d) = \frac{1}{n!} \prod_{k=1}^n \frac{\tau - d_2}{d_k} = \frac{(\tau - d_2)^n}{n! \prod d}$$

While the fractional volume  $v$  can still be expressed as the full simplex volume  $v_{(0,\dots,0)}$  minus the *total spillover volume* special care must now be taken in computing the spillover volume in terms of the individual *spillover simplex volumes*  $v_{(1,0,\dots)}$  and  $v_{(0,1,0,\dots)}$  due to the fact that the respective half-spaces given by  $z_1 > 1$  and  $z_2 > 1$  intersect within the quarter-space where both  $z_1, z_2 > 1$ . As such, the half-space spillover simplices may also intersect (which will be the case if  $\tau > d_1 + d_2$ ). If so, their intersection is yet another simplex within the  $z_1, z_2 > 1$  quarter-space with an orthogonal corner at  $(1,1,0,\dots)$  and edge lengths  $\frac{\tau-d_1-d_2}{d_k}$  along each  $z_i$  axis and with the following volume.

$$v_{(1,1,0,\dots)}(\tau, d) = \frac{1}{n!} \prod_{k=1}^n \frac{\tau - d_1 - d_2}{d_k} = \frac{(\tau - d_1 - d_2)^n}{n! \prod d}$$

Thus, summing the two half-space simplex volumes  $v_{(1,0,\dots)}$  and  $v_{(0,1,0,\dots)}$ ,  $v_{(0,\dots,0)}$  will yield the correct total spillover volume so long as the two spillover simplices do not intersect (which will be the case when  $\tau < d_1 + d_2$ ) but will otherwise end up double-counting the quarter-space simplex volume  $v_{(1,1,0,\dots)}$  which will therefore need to be subtracted in order to compute the total spillover volume.

A systematic pattern emerges as  $\tau$  continues to increase. One starts by computing the total simplex volume  $v_{(0,\dots,0)}$ . Then, for each  $k$  such that  $\tau > d_k$ , the corresponding half-space simplex volume  $v_{(\delta_{1k}, \dots, \delta_{nk})}$  (where  $\delta$  denotes the Kronecker delta) is subtracted, then for each  $j \neq k$  such that  $\tau > d_j + d_k$ , the corresponding quarter-space simplex volume  $v_{(\delta_{1j}+\delta_{1k}, \dots, \delta_{nj}+\delta_{nk})}$  is added to correct for having been over-subtracted by the two half-simplex volumes indexed by  $j$  and  $k$ . Then for each  $j \neq k \neq m$  such that  $\tau > d_j + d_k + d_m$ , the corresponding  $\frac{1}{8}$ -space simplex volume  $v_{(\delta_{1j}+\delta_{1k}+\delta_{1m}, \dots, \delta_{nj}+\delta_{nk}+\delta_{nm})}$  is subtracted to correct for a net over-addition by the three added quarter-simplex volumes associated with each of the two-index combinations  $jk$ ,  $jm$ , and  $km$  taken from the triplet  $jk m$  and the three subtracted half-simplex volumes associated with each of the one-index combinations  $j$ ,  $k$ , and  $m$  taken from the same triplet. Next, for each quadruplet of distinct indices such that  $\tau$  exceeds the sum of the respective elements of  $d$ , the corresponding  $\frac{1}{16}$ -space simplex volume is added to correct for the net over-subtraction by the four subtracted  $\frac{1}{8}$ -space simplex volumes associated with each triple-index combination from the quadruplet, by the added six quarter-simplex volumes associated with each double-index combination from the quadruplet, and by the subtracted four half-simplex volumes associated with each single-index combination from the quadruplet. The process of alternating subtraction and addition of simplex volumes continues until  $(n-1)$ -tuplets of indices have been accordingly processed. Note that the generic formula for simplex volumes to be added/subtracted at various stages in this process is as follows,

$$v_{z_{\text{vertex}}} = \frac{1}{n!} \prod_{k=1}^n \frac{\tau - d \cdot z_{\text{vertex}}}{d_k} = \frac{(\tau - d \cdot z_{\text{vertex}})^n}{n! \prod d}$$

where  $z_{\text{vertex}}$  denotes the vertex cell coordinates (all of which are 0 or 1) for the orthogonal corner of the corresponding spillover simplex (for half-space simplices a single coordinate will be 1, for quarter-space simplices two coordinates will be 1, and so on).

The entire algorithm can be summarized succinctly as follows:



1. Initialize the “running fractional volume”  $v$  to the volume of the full simplex with orthogonal corner at the cell origin as follows

$$v = \frac{\tau^n}{n! \prod d}$$

2. Now, looping from  $m=1$  to  $n-1$ :

- For each  $m$ -tuple of distinct (independent of order) indices  $k_1, \dots, k_m$  between 1 and  $n$ ,
- if  $\tau > d_{k_1} + d_{k_2} + \dots + d_{k_m}$  then update the running sum as follows

$$v = v + (-1)^m \frac{(\tau - d_{k_1} - d_{k_2} - \dots - d_{k_m})^n}{n! \prod d}$$

This procedure must be modified if any of the elements of the fractional directional increases vector  $d$  are zero (since the common denominator of all the simplex volumes would be zero in such cases). Fortunately, the modification is extremely simple. Namely, a reduced dimension vector  $\hat{d}$  is created by removing the zero entries of  $d$ , and the above procedure is then applied on  $\hat{d}$  (also substituting  $n$  as well for the reduced dimension  $\hat{n}$  of  $\hat{d}$ ) for the resulting set of lower-dimensional simplices.

#### 2.4.3. 3D fractional volume formulas

When applying this general strategy in 3D, it is helpful to note that there are 6 different transition points, as the total fractional increase  $\tau$  progresses along the unit interval, across which the formulas change. These transition values are given by  $\tau = d_1, d_2, d_3, d_1 + d_2, d_1 + d_3, d_2 + d_3$ , which divide the interval into seven subintervals, but this only represents one of two possible sorting orders. When sorting these transition values, the first two values will always be  $d_1$  and  $d_2$  and the last two values will always be  $d_1 + d_3$  and  $d_2 + d_3$  based on our prior assumption that  $d_1, d_2$ , and  $d_3$  are already sorted from smallest to largest to begin with. However, this initial sorting assumption is not enough to tell us anything about the relation between the middle two elements  $d_3$  and  $d_1 + d_2$ . As such, we will consider separate scenarios where  $d_1 + d_2 \leq d_3$  and where  $d_1 + d_2 > d_3$  (which is the same as  $d_3 \geq \frac{1}{2}$  and  $d_3 < \frac{1}{2}$  respectively since  $d_1 + d_2 + d_3 = 1$ ), thereby listing 8 possible subintervals even though only seven, at most, are applicable for any given set of fractional increases  $d_1, d_2$ , and  $d_3$ .

Applying the strategy and notation developed for the general case yields

$$v_{3D} = v_{(0,0,0)} - \begin{cases} 0, & [1] \quad 0 < \tau < d_1 \\ v_{(1,0,0)}, & [2] \quad d_1 < \tau < d_2 \\ v_{(1,0,0)} + v_{(0,1,0)}, & [3] \quad d_2 < \tau < d_3, d_1 + d_2 \\ v_{(1,0,0)} + v_{(0,1,0)} + v_{(0,0,1)}, & [4a] \quad d_3 < \tau < d_1 + d_2 \\ v_{(1,0,0)} + v_{(0,1,0)} - v_{(1,1,0)}, & [4b] \quad d_1 + d_2 < \tau < d_3 \\ v_{(1,0,0)} + v_{(0,1,0)} + v_{(0,0,1)} - v_{(1,1,0)}, & [5] \quad d_1 + d_2, d_3 < \tau < d_1 + d_3 \\ v_{(1,0,0)} + v_{(0,1,0)} + v_{(0,0,1)} - v_{(1,1,0)} \\ - v_{(1,0,1)}, & [6] \quad d_1 + d_3 < \tau < d_2 + d_3 \\ v_{(1,0,0)} + v_{(0,1,0)} + v_{(0,0,1)} - v_{(1,1,0)} \\ - v_{(1,0,1)} - v_{(0,1,1)}, & [7] \quad d_2 + d_3 < \tau < 1 \end{cases}$$

which, without any algebraic simplification (beyond factoring out the common denominator for each simplex

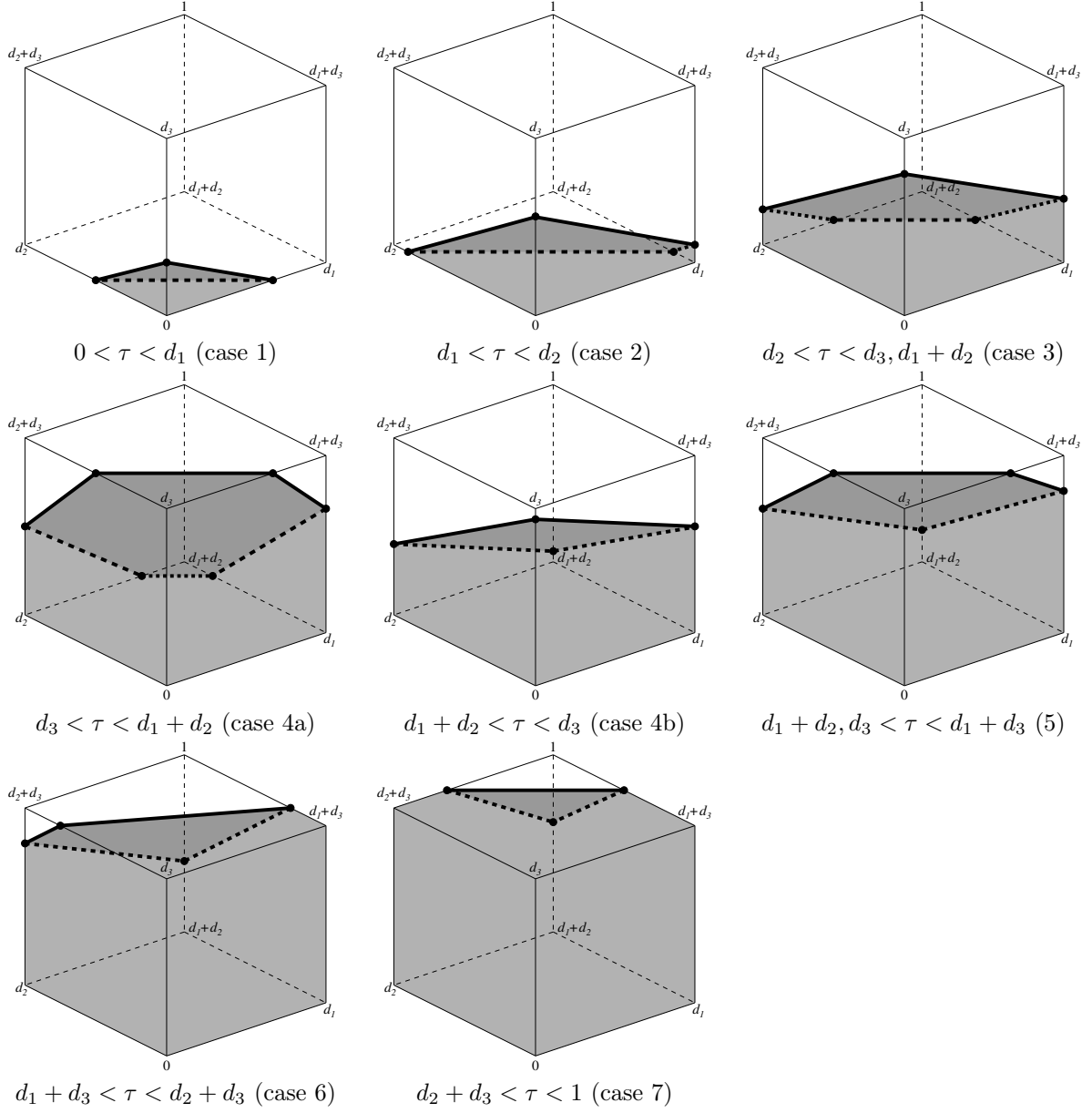


Figure 2: Different possible fractional 3D cell geometries

volume), results in the clearly patterned formula

$$\frac{1}{6d_1d_2d_3} \begin{cases} \tau^3, & 0 < \tau < d_1 \\ \tau^3 - (\tau - d_1)^3, & d_1 < \tau < d_2 \\ \tau^3 - (\tau - d_1)^3 - (\tau - d_2)^3, & d_2 < \tau < d_3, d_1 + d_2 \\ \tau^3 - (\tau - d_1)^3 - (\tau - d_2)^3 - (\tau - d_3)^3, & d_3 < \tau < d_1 + d_2 \\ \tau^3 - (\tau - d_1)^3 - (\tau - d_2)^3 & \\ \quad + (\tau - d_1 - d_2)^3, & d_1 + d_2 < \tau < d_3 \\ \tau^3 - (\tau - d_1)^3 - (\tau - d_2)^3 - (\tau - d_3)^3 & \\ \quad + (\tau - d_1 - d_2)^3, & d_1 + d_2, d_3 < \tau < d_1 + d_3 \\ \tau^3 - (\tau - d_1)^3 - (\tau - d_2)^3 - (\tau - d_3)^3 & \\ \quad + (\tau - d_1 - d_2)^3 + (\tau - d_1 - d_3)^3, & d_1 + d_3 < \tau < d_2 + d_3 \\ \tau^3 - (\tau - d_1)^3 - (\tau - d_2)^3 - (\tau - d_3)^3 & \\ \quad + (\tau - d_1 - d_2)^3 + (\tau - d_1 - d_3)^3 + (\tau - d_2 - d_3)^3, & d_2 + d_3 < \tau < 1 \end{cases}$$

Despite the simplicity of this pattern (and the resulting convenience in coding such case-by-case expressions through an accumulative loop instead), better numerical precision can be obtained, in situations where  $d_1$  and possibly even  $d_2$  are zero or close to zero, by using the following case-by-case algebraically simplified expressions (derived by exploiting  $d_1 + d_2 + d_3 = 1$ ) despite the loss of incremental looping convenience.

$$v_{3D}(\tau, d) = \begin{cases} \frac{\tau^3}{6d_1d_2d_3} = \frac{1}{6} \frac{\tau}{d_1} \frac{\tau}{d_2} \frac{\tau}{d_3}, & [1] \quad 0 \leq \tau < d_1 \\ \frac{d_1^2 + 3\tau(\tau - d_1)}{6d_2d_3} = \frac{1}{6} \frac{d_1}{d_2} \frac{d_1}{d_3} + \frac{1}{2} \frac{\tau - d_1}{d_2} \frac{\tau}{d_3}, & [2] \quad d_1 \leq \tau < d_2 \\ \frac{1}{2} + \frac{\tau - \frac{1}{2}}{d_3} + \frac{(1 - \tau - d_3)^3}{6d_1d_2d_3} = \dots \\ \quad \frac{\tau - \frac{d_1 + d_2}{2}}{d_3} + \frac{(1 - \tau - d_3)^3}{6d_1d_2d_3}, & [3] \quad d_2 \leq \tau < d_3, d_1 + d_2 \\ \frac{1}{2} + \frac{\tau - \frac{1}{2}}{d_3} + \frac{(1 - \tau - d_3)^3 - (\tau - d_3)^3}{6d_1d_2d_3} = \dots \\ \quad \frac{\tau - \frac{d_1 + d_2}{2}}{d_3} + \frac{(1 - \tau - d_3)^3 - (\tau - d_3)^3}{6d_1d_2d_3}, & [4a] \quad d_3 \leq \tau \leq d_1 + d_2 \quad [d_3 < d_1 + d_2] \\ \frac{1}{2} + \frac{\tau - \frac{1}{2}}{d_3} = \frac{\tau - \frac{d_1 + d_2}{2}}{d_3}, & [4b] \quad d_1 + d_2 \leq \tau \leq d_3 \quad [d_1 + d_2 \leq d_3] \\ \frac{1}{2} + \frac{\tau - \frac{1}{2}}{d_3} - \frac{(\tau - d_3)^3}{6d_1d_2d_3} = \dots \\ \quad \frac{\tau - \frac{d_1 + d_2}{2}}{d_3} - \frac{(\tau - d_3)^3}{6d_1d_2d_3}, & [5] \quad d_1 + d_2, d_3 < \tau \leq d_1 + d_3 \\ 1 - \frac{d_1^2 + 3(1 - \tau)(1 - \tau - d_1)}{6d_2d_3} = \dots \\ \quad 1 - \frac{1}{6} \frac{d_1}{d_2} \frac{d_1}{d_3} - \frac{1}{2} \frac{1 - \tau - d_1}{d_2} \frac{1 - \tau}{d_3}, & [6] \quad d_1 + d_3 < \tau \leq d_2 + d_3 \\ 1 - \frac{(1 - \tau)^3}{6d_1d_2d_3} = 1 - \frac{1}{6} \frac{1 - \tau}{d_1} \frac{1 - \tau}{d_2} \frac{1 - \tau}{d_3}, & [7] \quad d_2 + d_3 < \tau \leq 1 \end{cases}$$

The above formulae are well conditioned numerical expressions which do not cause numerical underflow or overflow as the individual components tend to zero. If instead we were to stick to the earlier patterned formulae, they would behave badly as  $d_1$   $d_2$  tend to zero. Notice that if  $d_1=0$ , then only cases 2, 4b, and 6 yield non-empty subintervals, and the resulting three formulas match those of the 2D fractional area with  $d_2$  and  $d_3 = 1 - d_2$  taking the place of  $d_1$  and  $d_2 = 1 - d_1$ . If  $d_2=0$  as well, then  $d_3=1$ , and only the 4b

subinterval is non-empty, and its formula matches  $\tau$  itself (the 1D fractional length).

$$v_{3D} \left( \tau, \begin{bmatrix} d_1=0 \\ d_2 \\ d_3 \end{bmatrix} \right) = v_{2D} \left( \tau, \begin{bmatrix} d_2 \\ d_3 \end{bmatrix} \right) \quad \text{and}$$

$$v_{3D} \left( \tau, \begin{bmatrix} d_1=0 \\ d_2=0 \\ d_3 \end{bmatrix} \right) = v_{2D} \left( \tau, \begin{bmatrix} d_2=0 \\ d_3 \end{bmatrix} \right) = v_{1D}(\tau)$$

### 2.5. Efficient computation of $M(T)$

We now numerically approximate the volume integral  $M(T)$  for each of the discretized level set values  $T = T_{\min}, T_{\min} + \Delta T, T_{\min} + 2\Delta T, \dots, T_{\max}$  by summing over all cell-wise integrals  $M_i(T)$

$$M(T) \approx \sum_i M_i(T) \tag{1a}$$

$$M_i(T) = h(x_i) \|\nabla \psi(x_i)\| \underbrace{\left( \prod \Delta x \right) v \left( \frac{T - \min \psi_i}{\max \psi_i - \min \psi_i}, \frac{D_i}{\|D_i\|_1} \right)}_{V_i(T)} \tag{1b}$$

computed according to the linear approximation  $\psi_i$  of  $\psi$  detailed in 2.2 and a constant approximation  $h_i = h(x_i)$  of  $h$  within each grid cell. While this mismatch in approximation order (only constant for  $h$  but linear for  $\psi$ ) may initially seem odd, it is justified by the fact that  $M(T)$  is defined by the volumetric integral of  $h \|\nabla \psi\|$ , and computation of this integrand minimally requires a constant approximation of  $h$  and a first-order approximation of  $\psi$  (which results in a constant approximation of the integrand  $h \|\nabla \psi\|$  itself).

Rather than visiting all the grid cells every time we sum  $M_i(T)$  for each discrete value of  $T$ , we may make the procedure more efficient by partitioning the entire set of grid cells into subsets according to whether their partial volumes  $V_i(T)$  are “full” (equal to the full cell volume), “empty” (equal to zero), or “strictly partial” (non-zero but less than the full cell volume). This partition will change as  $T$  increases, but the number of “full” cells can never decrease since such cells are characterized by  $\max \psi_i \leq T$ , while the number of “empty” cells can never increase since such cells are characterized by  $\min \psi_i \geq T$ . Since we may represent a single grid cell by its index  $i$ , we may accordingly represent all of the cells grouped within these classes via the following index sets

$$\begin{aligned} \mathcal{J}_{\text{full}}(T) &= \{i \mid \max \psi_i \leq T\} \\ \mathcal{J}_{\text{partial}}(T) &= \{i \mid \min \psi_i < T < \max \psi_i\} \\ \mathcal{J}_{\text{empty}}(T) &= \{i \mid \min \psi_i \geq T\} \\ \mathcal{J}_{\text{notfull}}(T) &= \{i \mid \max \psi_i > T\} = \mathcal{J}_{\text{partial}}(T) \cup \mathcal{J}_{\text{empty}}(T) \end{aligned}$$

where we have added a fourth class “not full” which represents cells that are either “empty” or “partial”.

The key point to exploit is that  $M_i$  becomes constant for increasing values of  $T$  once a cell becomes full. Thus, rather than computing  $M_i(T + \Delta T)$  for any of the cells in  $\mathcal{J}_{\text{full}}(T)$ , the following relationship may be used instead

$$\begin{aligned} \sum_i M_i(T + \Delta T) &= \sum_{i \in \mathcal{J}_{\text{full}}(T)} M_i(T + \Delta T) + \sum_{i \in \mathcal{J}_{\text{notfull}}(T)} M_i(T + \Delta T) \\ &= \underbrace{\sum_{i \in \mathcal{J}_{\text{full}}(T)} M_i(T)}_{M_{\text{full}}(T)} + \sum_{i \in \mathcal{J}_{\text{notfull}}(T)} M_i(T + \Delta T) \end{aligned}$$

where  $M_{\text{full}}(T)$  denotes the partial sum of  $M_i(T)$  over only the cells that were already full at the level set value  $T$ . So if we know  $M_{\text{full}}(T)$ , then we do not need to visit any of the  $\mathcal{J}_{\text{full}}(T)$  grid points to compute our approximation of  $M(T + \Delta T)$  by using the formula

$$\begin{aligned} M(T + \Delta T) &\approx \sum_i M_i(T + \Delta T) \\ &= M_{\text{full}}(T) + \sum_{i \in \mathcal{J}_{\text{notfull}}(T)} M_i(T + \Delta T) \end{aligned}$$

which only requires we visit the  $\mathcal{J}_{\text{notfull}}(T)$  grid points. Of course, in the process of visiting these  $\mathcal{J}_{\text{notfull}}(T)$  grid cells to compute their respective  $M_i(T + \Delta T)$  contributions, we may encounter grid cells that have now become full for  $T + \Delta T$ , thereby reducing the size of the updated set  $\mathcal{J}_{\text{notfull}}(T + \Delta T)$  of grid cells that remain unfilled. The partial sum  $M_{\text{full}}$  should therefore be updated as well

$$M_{\text{full}}(T + \Delta T) = M_{\text{full}}(T) + \sum_{\substack{i \in \mathcal{J}_{\text{notfull}}(t) \\ i \notin \mathcal{J}_{\text{notfull}}(T + \Delta T)}} M_i(T + \Delta T)$$

by adding the values of  $M_i(T + \Delta T)$  for the newly filled grid cells that were removed to create the updated  $\mathcal{J}_{\text{notfull}}(T + \Delta T)$  set.

#### 2.5.1. General traversal algorithm

Applying these iterative concepts yields the following algorithm

##### Initialize

1. Set  $M_{\text{full}}$  initially to zero
2. Put all grid indices in the initial list  $\mathcal{J}_{\text{notfull}}$
3. For each grid index  $i$ , compute and store  $\|\nabla\psi(x_i)\|$ ,  $\min\psi_i$ ,  $\max\psi_i$ , and the (sorted) relative increases  $d$

**Loop**  $T = T_{\min}$  through  $T = T_{\max}$  (by  $\Delta T$  steps)

1. Initialize  $M(T) = M_{\text{full}}$
2. For each index  $i$  within the list  $\mathcal{J}_{\text{notfull}}$ 
  - compute  $\Delta M = M_i(T) = (\prod \Delta x) h(x_i) \|\nabla\psi(x_i)\| v\left(\frac{T - \min\psi_i}{\max\psi_i - \min\psi_i}, \frac{D_i}{\|D_i\|_1}\right)$
  - increment  $M(T) = M(T) + \Delta M$
  - if  $\max\psi_i \leq T$  then also increment  $M_{\text{full}} = M_{\text{full}} + \Delta M$  and remove  $i$  from the list  $\mathcal{J}_{\text{notfull}}$

#### 2.5.2. Even more efficient strategy for distance functions

In the case where  $\psi$  represents a distance function to the  $T_{\min}$  level set or, more generally, a function for which it is possible to connect any domain point to the  $T_{\min}$  level set by a trajectory along which  $\psi$  changes monotonically, an even more efficient strategy can be developed. The idea here is to traverse the grid points monotonically with respect to  $\psi$ , much like what is done in fast marching algorithms (which are often employed to compute the level set function  $\psi$  itself). In this case, it is not necessary to visit all of the previously “empty cells” when computing  $M(T + \Delta T)$  since many of them will remain empty, and therefore contribute nothing to the sum. While this is also typically true in the general case outlined above, the lack of a causal monotonic structure makes it impossible to know which of the previously empty cells for  $t$  will remain empty for  $T + \Delta T$ . However, when the causal structure applies, we can be assured that the set of previously empty cells which become nonempty for the new level set value of  $T + \Delta T$  must be connected to the set of previously non-empty cells, thereby allowing us to devise a more efficient search strategy as follows.

### Initialize

1. Set  $M_{\text{full}}$  initially to zero
2. For each grid index  $i$ , compute and store  $\|\nabla\psi(x_i)\|$ ,  $\min\psi_i$ ,  $\max\psi_i$ , and the (sorted) relative increases  $d$
3. Put all grid indices for which  $\min\psi_i < T_{\min}$  in the initial list  $\mathcal{J}_{\text{partial}}$
4. Set a binary flag  $\text{visited}_i$  to one for each of these indices in the list, and set such a flag to zero for all remaining grid indices. We will refer to these two groups of indices as “visited” and “unvisited” respectively.

**Loop**  $T = T_{\min}$  through  $T = T_{\max}$  (by  $\Delta T$  steps)

1. Initialize  $M(T) = M_{\text{full}}$
2. Retrieving each index  $i$  sequentially from  $\mathcal{J}_{\text{partial}}$  until the end of the list is reached
  - compute  $\Delta M = M_i(T) = (\prod \Delta x) h(x_i) \|\nabla\psi(x_i)\| v\left(\frac{T - \min\psi_i}{\max\psi_i - \min\psi_i}, \frac{D_i}{\|D_i\|_1}\right)$
  - increment  $M(T) = M(T) + \Delta M$
  - Append any “unvisited neighbor index”  $j$  (meaning that  $x_j$  is a neighbor of  $x_i$  in the Cartesian grid and that  $\text{visited}_j=0$ ) for which  $\min\psi_j < T$  to the *end* of the list  $\mathcal{J}_{\text{partial}}$  and then toggle the flag  $\text{visited}_j=1$ .
  - if  $\max\psi_i \leq T$  then also increment  $M_{\text{full}} = M_{\text{full}} + \Delta M$  and remove  $i$  from the list  $\mathcal{J}_{\text{partial}}$  (and append any still unvisited neighbor index  $j$  to  $\mathcal{J}_{\text{partial}}$  and then toggle the flag  $\text{visited}_j=1$ )

Note that the sequential traversal of the  $\mathcal{J}_{\text{partial}}$  list in step 2 is important since the list will potentially grow as it is being traversed, with additional elements being appended to the end of the list. If the list is not traversed sequentially (or if appending does not occur at the end of the list) then the additional elements may not be processed as they should be during the traversal.

### 2.6. Direct computation of $m(T)$

The level set integrals  $m(T)$  of  $h$  for each discretized level set value  $T$  are obtained by differentiating the antiderivative function  $M(T)$  which we have constructed thusfar. This may be done numerically, by first computing the discrete representation of  $M(T)$  at  $T = T_{\min}, T_{\min} + \Delta T, \dots, T_{\max}$ , and then taking the numerical differences between consecutive samples (and dividing by  $\Delta T$ ). However, given that the approximation 1a for  $M$  consists of the sum of analytically differentiable elements  $M_i(T)$ , one may instead approximate the function  $m$  directly by differentiating the elements  $M_i$  inside the sum. The sum of the resulting elements  $m_i(T)$  may then be used to directly approximate the function  $m$  of level set integrals.

$$m(T) = \frac{d}{dT} M(T) \approx \frac{d}{dT} \sum_i M_i(T) = \sum_i m_i(T)$$

These differentiated elements  $m_i$  may be expressed as follows

$$\begin{aligned} m_i(T) &= \dot{M}_i(T) \\ &= \left( \prod \Delta x \right) h(x_i) \|\nabla\psi(x_i)\| \frac{d}{dT} v\left( \underbrace{\frac{T - \min\psi_i}{\max\psi_i - \min\psi_i}}_{\tau}, \underbrace{\frac{D_i}{\|D_i\|_1}}_d \right) \\ &= \left( \prod \Delta x \right) h(x_i) \frac{\|\nabla\psi(x_i)\|}{\max\psi_i - \min\psi_i} \underbrace{\frac{\partial v}{\partial \tau} \left( \frac{T - \min\psi_i}{\max\psi_i - \min\psi_i}, \frac{D_i}{\|D_i\|_1} \right)}_{\text{differential fractional volume}} \end{aligned}$$

where the partial derivative  $\frac{\partial v}{\partial \tau}$  represents the differential fractional volume within the unit cell. We obtain this analytically by differentiating the expressions for the fractional volume  $v$  presented earlier (the 2D and 3D cases are presented below). The surface area (arclength in 2D) element  $dA(T)$  for the  $T$ -level set of  $\psi$  is therefore approximated within the cell by the intersected area  $A_i(T)$  of the  $T$ -level hypersurface of  $\psi_i$  (intersected length in 2D) given as follows,

$$A_i(T) = \left( \prod \Delta x \right) \frac{\|\nabla \psi(x_i)\|}{\max \psi_i - \min \psi_i} \frac{\partial v}{\partial \tau} \left( \frac{T - \min \psi_i}{\max \psi_i - \min \psi_i}, \frac{D_i}{\|D_i\|_1} \right)$$

yielding the following intuitive expression for the level set integral cell-wise elements  $m_i$ .

$$m_i(T) = h(x_i) A_i(T)$$

### 2.6.1. 2D differential fractional volume (area)

The differential fractional volume  $\frac{\partial v}{\partial \tau}$  in 2D (where it is actually better interpreted as a “differential fractional area”) is given as follows,

$$\frac{\partial v_{2D}}{\partial \tau}(\tau, d) = \frac{1}{d_2} \begin{cases} \frac{\tau}{d_1}, & 0 \leq \tau < d_1 \\ 1, & d_1 \leq \tau \leq 1 - d_1 \\ \frac{1-\tau}{d_1}, & 1 - d_1 < \tau < 1 \end{cases}$$

with  $\frac{\partial v_{2D}}{\partial \tau} = 0$  for any other value of  $\tau$  outside the interval  $[0, 1]$ .

### 2.6.2. 3D differential fractional volume

The differential fractional volume  $\frac{\partial v}{\partial \tau}$  in 3D is given as follows.

$$\frac{\partial v_{3D}}{\partial \tau}(\tau, d) = \frac{1}{d_3} \begin{cases} \frac{\tau^2}{2d_1 d_2}, & [1] \quad 0 \leq \tau < d_1 \\ \frac{\tau - \frac{1}{2}d_1}{d_2}, & [2] \quad d_1 \leq \tau < d_2 \\ 1 - \frac{(1-\tau-d_3)^2}{2d_1 d_2}, & [3] \quad d_2 \leq \tau < d_3, d_1 + d_2 \\ 1 - \frac{(1-\tau-d_3)^2 + (\tau-d_3)^2}{2d_1 d_2}, & [4a] \quad d_3 \leq \tau \leq d_1 + d_2 \quad [d_3 < d_1 + d_2] \\ 1, & [4b] \quad d_1 + d_2 \leq \tau \leq d_3 \quad [d_1 + d_2 \leq d_3] \\ 1 - \frac{(\tau-d_3)^2}{2d_1 d_2}, & [5] \quad d_1 + d_2, d_3 < \tau \leq d_1 + d_3 \\ \frac{(1-\tau) - \frac{1}{2}d_1}{d_2}, & [6] \quad d_1 - d_3 < \tau \leq d_2 + d_3 \\ \frac{(1-\tau)^2}{2d_1 d_2}, & [7] \quad d_2 + d_3 < \tau \leq 1 \end{cases}$$

with  $\frac{\partial v_{3D}}{\partial \tau} = 0$  for any other value of  $\tau$  outside the interval  $[0, 1]$ .

### 3. Experimental results

In this section we present some numerical experimental results. Note that, our method is fundamentally designed to compute a whole family of integrals efficiently in a coupled way but nevertheless it is instructive to compare our accuracy to traditional single isosurface methods designed to perform integration along specific level surfaces. In a later sub-section we show more relevant experiments by computing integrals along families of isosurfaces. Here we compare our method to the Geometric numerical integration method of Min-Gibou [15]. In [15], the authors had compared their Geometric numerical integration method to that of the first-order and second-order Delta function formulation [11]. Comparisons were made on accounts of robustness to perturbations of the interface location on the grid, order of convergence and numerical accuracy. We present our results together with that of [15] and [11], effectively comparing all four methods. Through experiments in both 2D and 3D domains, we demonstrate that our methods achieve similar levels of accuracy to traditional single isosurface methods while providing the advantage of being able to compute integrals along entire sets of level surfaces efficiently in a coupled way. We conduct all our experiments on a computer with a quad-core Intel core i7 CPU with 16 GB available RAM and we implemented our methods in the C++ programming language.

#### 3.1. Experiments in 2D

In this section we compute the arc-length an ellipse represented as the zero level set of  $\phi(x, y) = \frac{x^2}{1.5^2} + \frac{y^2}{0.75^2} - 1$  on a two dimensional grid spanning the range  $[-5, 5]$  in both dimensions. The true arc-length of this ellipse is  $\approx 7.266336165$  [11]. We used numerical implementation of our algorithm to experimentally compute the arc-length of the ellipse for various isotropic grid resolutions( $\Delta x$ ) going from coarse resolution of 0.2 to much finer grid resolution of 0.0625. Similar to the experiments in [15], we conducted 50 trials where the ellipse was randomly translated on the grid. We generated a set of 50 pairs of uniform random numbers in the range of  $[0, 1)$  and used them as the center of the ellipse which effectively shifted the location of the interface on the grid. We used this same set of center perturbations for all grid resolutions( $\Delta x$ ). 1 shows the data for calculating the arc-length of the ellipse, averaged over 50 trials for each grid resolution. In order to compare our computation to the true arc-length of the ellipse we calculate the relative error for each trial and then compute the average relative error over the 50 trials for each grid resolution. We also compute additional statistics such as the minimum(Min) and maximum(Max) relative error and its standard deviation(SD). Finally, we also show the experimental order of convergence(Ord) as we get finer grid resolutions and also show the ratio of the maximum and minimum relative error(Max/Min) over all 50 trials for a grid resolution. The order of convergence is calculated as  $\log_2 \left( \frac{E_k}{E_{k+1}} \right) / \log_2 \left( \frac{\Delta x^k}{\Delta x^{k+1}} \right)$  where  $E_k$  is the quantity under consideration for e.g. average relative error at a particular grid resolution level indicated by  $k$ .

As we can see from 1, the average relative error in calculating the arc-length of the ellipse is very similar to the Geometric Integration approach of Min-Gibou. On some accounts, such as minimum error, our approach performs better while in other cases such maximum-to-minimum ratio it is slightly worse. Overall, we see however the comparable accuracy to earlier single isosurface integration methods(although not the intended use of our methods).

#### 3.2. Experiments in 3D

In this section we compute the surface area and volume of an ellipsoid represented as the zero level set of  $\phi(x, y, z) = \frac{x^2}{1.5^2} + \frac{y^2}{0.75^2} + \frac{z^2}{0.5^2} - 1$ . The true surface area of this ellipsoid is  $\approx 9.901821$  [11]. Similar to the experiments in [15] and our experiments in 2D as shown in last sub-section, we conducted 50 trials where the ellipsoid was randomly translated on the grid. This time we generate a triplet of uniform random numbers in range  $[0, 1)$  to perturb the center of the ellipsoid in order to shift the location of its interface on the grid. We again use this same set of 50 random translations for all grid resolutions and compute similar statistics related to the relative error as we did in the 2D case. 2 shows these statistics for calculating the surface area of the ellipsoid. As we can see our algorithm is much more robust to grid perturbations in 3D than in 2D as indicated by the low Max/Min errors (last column). It is more robust than the first and



Table 1: Computing arc-length of an ellipse for various grid resolutions for 50 trials

| $\Delta x$                                | Average  | Order | SD       | Min      | Order | Max      | Order | $\frac{max}{min}$ |
|---|----------|-------|----------|----------|-------|----------|-------|-------------------|
| Intrinsic Integration                     |          |       |          |          |       |          |       |                   |
| 0.2                                       | 2.95E-03 | 0.00  | 2.11E-03 | 3.87E-06 | 0.00  | 1.04E-02 | 0.00  | 2684.60           |
| 0.1                                       | 1.04E-03 | 1.51  | 5.84E-04 | 1.04E-04 | -4.74 | 2.25E-03 | 2.21  | 21.71             |
| 0.05                                      | 3.04E-04 | 1.77  | 1.80E-04 | 1.65E-05 | 2.65  | 6.24E-04 | 1.85  | 37.87             |
| 0.025                                     | 8.90E-05 | 1.77  | 6.35E-05 | 3.00E-07 | 5.78  | 2.36E-04 | 1.40  | 786.26            |
| 0.0125                                    | 3.12E-05 | 1.51  | 2.52E-05 | 8.54E-07 | -1.51 | 1.20E-04 | 0.98  | 140.59            |
| 0.00625                                   | 1.29E-06 | 1.28  | 9.40E-06 | 2.25E-07 | 1.93  | 2.99E-05 | 2.00  | 133.36            |
| Min-Gibou [15]                            |          |       |          |          |       |          |       |                   |
| 0.2                                       | 5.04E-03 | 0.00  | 2.15E-04 | 4.63E-03 | 0.00  | 5.49E-03 | 0.00  | 1.19              |
| 0.1                                       | 1.26E-03 | 2.00  | 3.23E-05 | 1.17E-03 | 1.99  | 1.30E-03 | 2.08  | 1.11              |
| 0.05                                      | 3.14E-04 | 2.00  | 6.61E-06 | 3.03E-04 | 1.95  | 3.26E-04 | 2.00  | 1.08              |
| 0.025                                     | 7.84E-05 | 2.00  | 1.25E-06 | 7.50E-05 | 2.02  | 7.99E-05 | 2.03  | 1.07              |
| 0.0125                                    | 1.96E-05 | 2.00  | 2.15E-07 | 1.90E-05 | 1.98  | 1.99E-05 | 2.01  | 1.04              |
| 0.00625                                   | 4.90E-06 | 2.00  | 3.18E-08 | 4.83E-06 | 1.98  | 4.94E-06 | 2.01  | 1.02              |
| First-order delta function approach [11]  |          |       |          |          |       |          |       |                   |
| 0.2                                       | 8.96E-03 | 0.00  | 7.93E-03 | 1.28E-04 | 0.00  | 2.67E-02 | 0.00  | 208               |
| 0.1                                       | 2.70E-03 | 1.73  | 2.96E-03 | 9.13E-05 | 1.31  | 1.07E-02 | 0.49  | 118               |
| 0.05                                      | 9.55E-04 | 1.50  | 1.12E-03 | 4.19E-07 | 1.28  | 4.43E-03 | 7.77  | 10600             |
| 0.025                                     | 3.21E-04 | 1.57  | 3.58E-04 | 7.32E-06 | 1.54  | 1.52E-03 | -4.12 | 208               |
| 0.0125                                    | 1.13E-04 | 1.51  | 1.22E-04 | 9.15E-06 | 1.53  | 5.28E-04 | -0.32 | 57.7              |
| 0.00625                                   | 3.94E-05 | 1.52  | 4.17E-05 | 2.01E-06 | 1.52  | 1.84E-04 | 2.19  | 91.7              |
| Second-order delta function approach [11] |          |       |          |          |       |          |       |                   |
| 0.2                                       | 3.23E-03 | 0.00  | 2.74E-03 | 6.07E-04 | 0.00  | 1.30E-02 | 0.00  | 21.5              |
| 0.1                                       | 5.74E-04 | 2.49  | 5.25E-04 | 2.93E-06 | 7.69  | 3.02E-03 | 2.10  | 1030              |
| 0.05                                      | 1.13E-04 | 2.34  | 4.08E-05 | 2.55E-05 | 3.12  | 2.04E-04 | 3.88  | 8.01              |
| 0.025                                     | 3.08E-05 | 1.87  | 8.31E-06 | 1.56E-05 | 0.70  | 4.72E-05 | 2.11  | 3.00              |
| 0.0125                                    | 7.61E-06 | 2.01  | 1.51E-06 | 1.37E-06 | 3.50  | 1.21E-05 | 1.96  | 8.82              |
| 0.00625                                   | 1.89E-06 | 2.01  | 1.82E-07 | 1.61E-06 | 0.23  | 2.12E-06 | 2.45  | 1.37              |

second order delta formulations and close to Min-Gibou method. The results are also close to second order accurate, closer to the method of Min-Gibou and better than the first and second order delta formulations. Finally, in 3 we compute the volume of the same ellipsoid and compare the average relative errors to the Geometric Integration method. Again, we can see that our method is very competitive both in terms of accuracy and order of convergence. In this case, we conduct only one trial without any center perturbations.

Table 2: Computing surface area of an ellipsoid for various grid resolutions for 50 trials

| $\Delta x$                       | Average  | Order | SD       | Min      | Order | Max      | Order | $\frac{max}{min}$ |
|----------------------------------|----------|-------|----------|----------|-------|----------|-------|-------------------|
| Intrinsic Integration            |          |       |          |          |       |          |       |                   |
| 0.2                              | 2.15E-02 | 0.00  | 2.85E-03 | 1.57E-02 | 0.00  | 2.91E-02 | 0.00  | 1.85              |
| 0.1                              | 5.27E-03 | 2.03  | 1.04E-03 | 2.88E-03 | 2.45  | 7.75E-03 | 1.91  | 2.70              |
| 0.05                             | 1.36E-03 | 1.96  | 3.07E-04 | 4.93E-04 | 2.55  | 1.83E-03 | 2.09  | 3.71              |
| 0.025                            | 3.24E-04 | 2.07  | 4.23E-05 | 2.34E-04 | 1.07  | 4.38E-04 | 2.06  | 1.87              |
| Min-Gibou [15]                   |          |       |          |          |       |          |       |                   |
| 0.2                              | 3.17E-02 | 0.00  | 2.90E-04 | 3.12E-02 | 0.00  | 3.22E-02 | 0.00  | 1.03              |
| 0.1                              | 7.91E-03 | 1.98  | 1.02E-05 | 7.89E-03 | 1.98  | 7.94E-03 | 2.02  | 1.00              |
| 0.05                             | 1.98E-03 | 2.00  | 6.81E-07 | 1.98E-03 | 2.00  | 1.98E-03 | 2.00  | 1.00              |
| 0.025                            | 4.94E-04 | 2.00  | 1.13E-07 | 4.94E-04 | 2.00  | 4.95E-04 | 2.00  | 1.00              |
| First-order delta approach [11]  |          |       |          |          |       |          |       |                   |
| 0.2                              | 3.03E-02 | 0.00  | 7.12E-03 | 1.75E-02 | 0.00  | 4.73E-02 | 0.00  | 1.49              |
| 0.1                              | 7.77E-03 | 1.96  | 2.26E-03 | 3.95E-03 | 2.14  | 1.32E-03 | 1.84  | 1.51              |
| 0.05                             | 2.12E-03 | 1.87  | 7.36E-04 | 6.39E-04 | 2.62  | 4.48E-03 | 1.56  | 2.16              |
| 0.025                            | 5.20E-04 | 2.03  | 1.36E-04 | 3.41E-04 | 0.91  | 8.51E-04 | 2.39  | 1.54              |
| Second-order delta approach [11] |          |       |          |          |       |          |       |                   |
| 0.2                              | 6.86E-02 | 0.00  | 7.60E-02 | 1.01E-02 | 0.00  | 4.46E-01 | 0.00  | 44.4              |
| 0.1                              | 1.33E-02 | 2.37  | 8.38E-03 | 9.47E-04 | 3.41  | 2.91E-02 | 3.93  | 3.08              |
| 0.05                             | 2.60E-03 | 2.35  | 2.11E-03 | 2.49E-04 | 1.92  | 1.06E-02 | 1.45  | 42.4              |
| 0.025                            | 8.00E-04 | 1.70  | 1.01E-03 | 4.40E-06 | 5.82  | 6.88E-03 | 0.62  | 1570              |

Table 3: Convergence rate for computing volume of ellipsoid for various grid resolutions for one trial. Relative error and order of convergence shown for our method and that of Min-Gibou

| $\Delta x$ | Intrinsic Integration | Order | Min-Gibou | order |
|------------|-----------------------|-------|-----------|-------|
| 0.1        | 1.04E-02              | 0.00  | 1.36E-02  | 0.00  |
| 0.05       | 2.59E-03              | 2.00  | 3.40E-03  | 2.00  |
| 0.025      | 6.48E-04              | 2.00  | 8.50E-04  | 2.00  |

### 3.3. Computing families of integrals

In the last two sub-sections we presented some results and comparisons for computing integrals along a single levelset of a function. We did that with the aim of demonstrating that our method achieves accuracy similar to traditional single isocontour methods even though developed with aim of computing a whole family of integrals in one shot in contrast to these traditional methods. In this sub-section we show that our techniques allows simultaneous and coupled computation of families of integrals while offering significant computational advantages.

In this experiment, we compute the arc length of whole families of level curves of a circle represented as the zero level set of  $\phi(x, y) = x^2 + y^2 - 1$  on a grid spanning the range  $[-5, 5]$  in both X and Y directions with an isotropic grid resolution  $\Delta x = 0.025$ . We compute the arc lengths of progressively expanding circles corresponding to level curve represented by  $T_{min} = -0.5$  to  $T_{max} = 2.0$ . We divide the range  $[T_{min}, T_{max}]$  into  $nTs$  equally spaced intervals with  $nTs$  ranging from 5 to 200 in increments of 5. We then employ

the two algorithms detailed in 2.5.1 and 2.5.2. We refer to the method of 2.5.1 as “Coupled Non-Causal Integration” and the method of 2.5.2 which applies to the special case of distance functions as “Coupled Causal Integration”. We compare the accuracy and speed of our methods with a brute-force approach of using the standard marching triangles based explicit isosurfacing technique in a sequential manner, one at a time over all the desired sub-level surfaces.

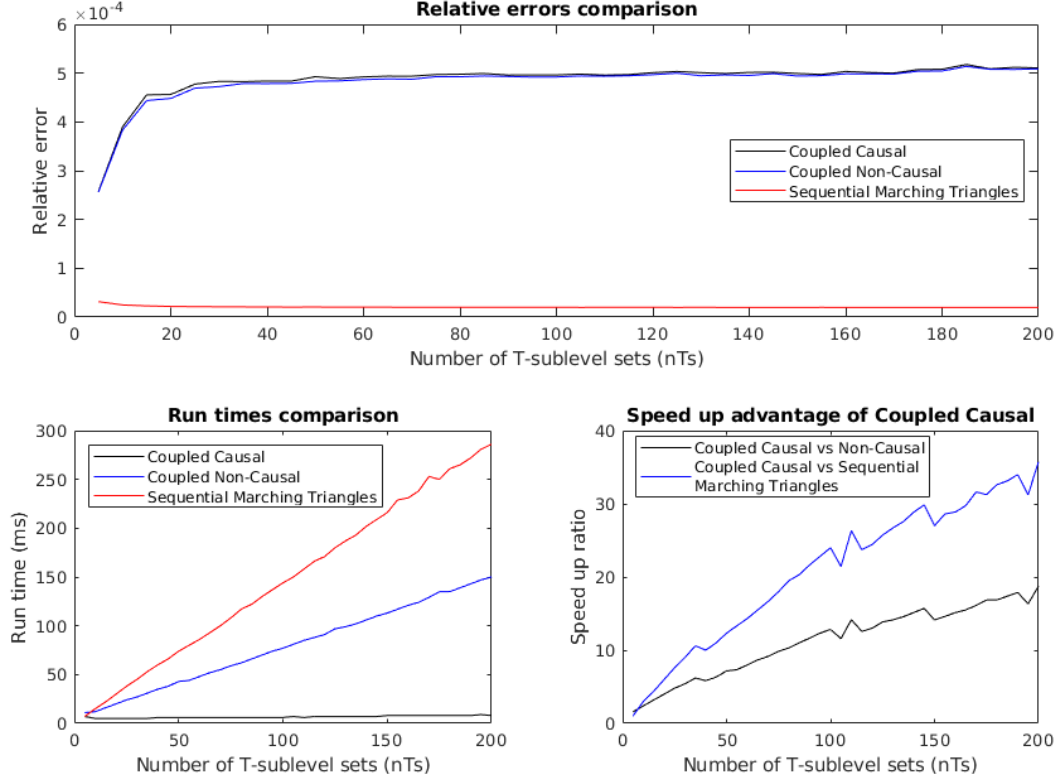


Figure 3: Accuracy(top) and run times(bottom) comparison of integration methods based on the experimental setup described in 3.3. The accuracy (relative error) of sequential marching triangle is approximately  $10^{-05}$  on average compared to our two methods at  $10^{-04}$ . In terms of run times comparison(bottom left), our methods specially designed to compute integrals along families of T sub-level curves/surfaces significantly outperform the application of standard marching triangles sequentially to each of the  $nTs$  sub-level curves. In terms of computational speed up(bottom right), in the special case of integration along signed distance functions and when the number of T sub-level curves are very large, our Coupled Causal method(2.5.2) delivers a speed up of approximately 15 times compared to our Coupled Non-Causal method(2.5.1) and approximately 35 times compared to sequential application of standard marching triangle approach to all the  $nTs$  sub-level curves.

In 3 top row, we compare the relative errors in computing the arc-length of expanding concentric circles using our two methods and marching triangles based explicit isosurfacing scheme. We take the average of the relative errors for each sub level curve  $\tau \in [T_{min}, T_{max}]$ . We can see that the accuracy of marching triangles is higher at the order of approximately  $10^{-05}$ . However, our two methods are also not far behind at approximately  $10^{-04}$ . The main advantage is in the computational efficiency of our methods compared to traditional methods. In 3 bottom left, we can see that the run time of both our methods is consistently lower than marching triangles based approach. The run times of the Coupled Causal method which applies to distance functions is significantly lower than either of the other methods. Finally, in 3 bottom right, we can see that as the number of T-level surfaces over which integration is performed increases, the Coupled Causal method can provide significant computational speed up while maintaining relatively good accuracy. Compared to the Coupled Non-Causal traversal algorithm, it can speed up the calculation of integrals by

15 - 20 times and almost 25 - 35 times when compared to Marching Triangles based approach. The Coupled Causal algorithm runs in almost constant time even as the number of integrals grows.

### 3.4. Practical Application

Identifying the precise location and extent of an object in an image is a fundamental task in many computer vision applications. Prior knowledge about the objects of interest may improve segmentation performance in the presence of noise, occlusion, and model errors. A review of these *recognition*-segmentation approaches with different priors, such as color, motion, shape, and texture is given in [24]. Shape is a powerful feature for many applications, particularly for medical imaging where shapes of body parts do not vary much among patients. Shape models are plentiful but most relevant to our work are level set representations of shape, which have been incorporated as shape priors for active contour techniques, e.g. in [25, 26, 8].

Additional robustness can be achieved when combining shape with appearance. Examples of level set approaches are [27, 28, 29] where principal component analysis (PCA) is performed on the level sets and on the pixel-intensity image of the training set to obtain coupled shape and appearance models. These approaches typically require computationally expensive two-dimensional warps of intensity templates to migrate between different shape configurations. Utilizing the computationally efficient intrinsic integration approach developed in this paper, we can propose a smaller, transformed set of intensity features (a one-dimensional function) by numerically integrating image intensities along iso-contours of the object's shape.

Given an image  $I$  and the object boundary shape  $C$  (and its equivalent signed-distance function  $\psi$ ), traditional appearance models build a two-dimensional image template. Instead, we propose to use the mean image intensities along iso-contours of the object shape, i.e., our one-dimensional template is defined as

$$f(T) = \frac{\int_{C_T} I ds}{\text{length}(C_T)}, \quad (2)$$

where  $f: [\psi_{\min}, 0] \mapsto \mathbb{R}$  are the mean intensities and  $C_T = \{x : \psi(x) = T\}$  are the iso-contours. In Figure 4, these quantities are illustrated for the image of a truck from the Berkeley Motion Segmentation dataset [30]. The level sets  $C_T$  for some values of  $T$  between  $\psi_{\min}$  and 0 are shown in Figure 4a and the mean intensity along these curves is plotted in Figure 4b.

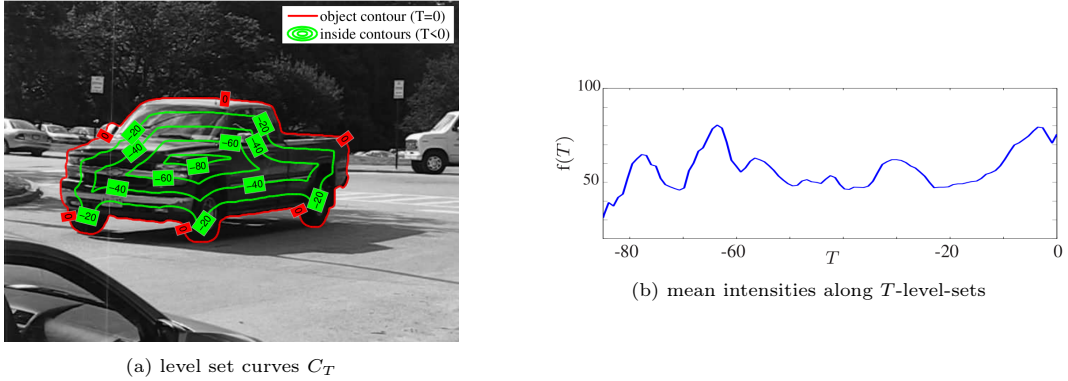


Figure 4: Illustration of the photo-geometric representation.

We call  $f(T)$  the coupled *photo-geometric* representation of an object because it couples the object's geometric information  $C_T$  with its photometric information  $I$ . As a feature, it is well-suited for training purposes because it is invariant to translation and rotation. It is also invariant to scale if the domain of  $f(T)$  is normalized to a constant interval, e.g.,  $[-1, 0]$ . As an appearance model, the photo-geometric representation can be viewed as a compromise between the powerful but cumbersome Active appearance models [31] and efficient but less discriminative methods, e.g., Chan-Vese [32] where object intensity is modeled through a finite set of statistics. Our proposed algorithm using the one-dimensional photo-geometric descriptor is more

general than finite sets of statistics, and at the same time not as cumbersome as two-dimensional template models.

A key point to note is that in order to compute this *photo-geometric* feature representation, we need to integrate over a number of level sets of an input image shape. There can be a multitude of training images and computing these features using traditional techniques applied sequentially to each level set will be extremely computationally expensive. In this case, we can apply our Coupled-Causal intrinsic integration technique (sec. 3.3) to compute the whole family of required integrals for each image in one shot. In the supplemental section, we show a complete development and implementation of a PCA based coupled shape and appearance model using the *photo-geometric* feature descriptor, efficiently computed using our integration techniques.

#### 4. Conclusions

In this paper, we have presented a method of computing an entire continuous family of integrals over a whole family of T-level surfaces of a function by making use of the coarea formula. We have presented several experiments to show that our method is still comparable to traditional single isosurface integration methods in terms of accuracy achieved while making possible the task of computing whole family of integrals in a simultaneous efficiently coupled way. We additionally presented a special method applicable to integration over distance functions which provides significant speed up over other traditional single isocontour/surface methods while still maintaining comparable accuracy. Our methods can find applications over many problem domains but particularly Active Contour(Surface) based methods routinely used in Computer Vision problems.

## References

- [1] S. Osher, J. A. Sethian, Fronts propagating with curvature-dependent speed: Algorithms based on hamilton-jacobi formulations, *Journal of Computational Physics* 79 (1) (1988) 12–49.
- [2] S. Osher, R. Fedkiw, *Level Set Methods and Dynamic Implicit Surfaces*, Springer, New York, 2003.
- [3] J. A. Sethian, *Level Set Methods and Fast Marching Methods: Evolving Interfaces in Geometry, Fluid Mechanics, Computer Vision, and Materials Sciences*, Cambridge University Press, Cambridge, UK, 1999.
- [4] J. A. Sethian, P. Smereka, Fronts propagating with curvature-dependent speed: Algorithms based on hamilton-jacobi formulations, *Annual Review of Fluid Mechanics* 35 (1) (2003) 341–372.
- [5] S. J. Osher, F. Santosa, Level set methods for optimization problems involving geometry and constraints: I. frequencies of a two-density inhomogeneous drum, *J. of Comp. Phys.* 171 (1) (2001) 272–288.
- [6] E. Maitre, F. Santosa, Level set methods for optimization problems involving geometry and constraints ii. optimization over a fixed surface, *J. of Comp. Phys.* 227 (22) (2008) 9596–9611.
- [7] D. Cremers, Dynamical statistical shape priors for level set-based tracking, *J. of Comp. Phys.* 28 (8) (2006) 1262–1273.
- [8] A. Tsai, A. Yezzi, W. Wells, C. Tempny, D. Tucker, A. Fan, W. E. Grimson, A. Willsky, A shape-based approach to the segmentation of medical imagery using level sets, *IEEE Transactions on Medical Imaging* 22 (2003) 137–154.
- [9] A.-K. Tornberg, B. Enquist, Numerical approximations of singular source terms in differential equations, *Journal of Computational Physics* 200 (2) (2004) 462–488.
- [10] B. Enquist, A.-K. Tornberg, R. Tsai, Discretization of dirac delta functions in level set methods, *Journal of Computational Physics* 207 (1) (2005) 28–51.
- [11] P. Smereka, The numerical approximation of a delta function with application to level set methods, *Journal of Computational Physics* 211 (1) (2006) 77–90.
- [12] W. E. Lorensen, H. E. Cline, Marching cubes: A high resolution 3d surface construction algorithm, *SIGGRAPH Computer Graphics* 21 (4) (1987) 163–169.
- [13] S. Chan, E. Purisima, A new tetrahedral tessellation scheme for isosurface generation, *Computers & Graphics* 22 (1) (1998) 83–90. doi:[https://doi.org/10.1016/S0097-8493\(97\)00085-X](https://doi.org/10.1016/S0097-8493(97)00085-X).
- [14] A. Gueziec, R. Hummel, Exploiting triangulated surface extraction using tetrahedral decomposition, *IEEE Transactions on Visualization and Computer Graphics* 1 (4) (1995) 328–342.
- [15] C. Min, F. Gibou, Geometric integration over irregular domains with application to level-set methods, *Journal of Computational Physics* 226 (2) (2007) 1432–1443.
- [16] B. Müller, F. Kummer, M. Oberlack, Y. Wang, Simple multidimensional integration of discontinuous functions with application to level set methods, *Journal of Computational Physics* 92 (7) (2012) 637–651.
- [17] B. Müller, F. Kummer, M. Oberlack, Highly accurate surface and volume integration on implicit domains by means of moment fitting, *Journal of Computational Physics* 96 (8) (2013) 512–528.
- [18] R. I. Saye, High-order quadrature methods for implicitly defined surfaces and volumes in hyperrectangles, *SIAM Journal on Scientific Computing* 37 (2) (2015) 993–1019.
- [19] C. Kublik, N. M. Tanushev, R. Tsai, An implicit interface boundary integral method for poisson’s equation on arbitrary domains, *J. of Comp. Phys.* 247 (2013) 279–311.
- [20] C. B. Macdonald, S. J. Ruuth, Level set equations on surfaces via the closest point method, *Journal of Scientific Computing* (2008).
- [21] S. J. Ruuth, B. Merriman, A simple embedding method for solving partial differential equations on surfaces, *J. Comput. Phys.* 227 (3) (2008) 1943–1961. doi:[10.1016/j.jcp.2007.10.009](https://doi.org/10.1016/j.jcp.2007.10.009).
- [22] C. Kublik, R. Tsai, Integration over curves and surfaces defined by the closest point mapping, *Research in the mathematical sciences* 3 (3) (2016).
- [23] C. Kublik, R. Tsai, An extrapolative approach to integration over hypersurfaces in the level set framework, *Mathematics of Computation* (2018).
- [24] D. Cremers, M. Rousson, R. Deriche, A review of statistical approaches to level set segmentation: Integrating color, texture, motion and shape, *International Journal of Computer Vision* 72 (2) (2007) 195–215.
- [25] X. Bresson, P. Vandergheynst, J.-P. Thiran, A variational model for object segmentation using boundary information and shape prior driven by the mumford-shah functional, *International Journal of Computer Vision* 68 (2006) 145–162.
- [26] M. E. Leventon, W. E. L. Grimson, O. Faugeras, Statistical shape influence in geodesic active contours, in: *Proceedings IEEE Conference on Computer Vision and Pattern Recognition. CVPR 2000 (Cat. No.PR00662)*, Vol. 1, 2000, pp. 316–323 vol.1. doi:[10.1109/CVPR.2000.855835](https://doi.org/10.1109/CVPR.2000.855835).
- [27] K. Fritscher, A. Grünerbl, R. Schubert, 3d image segmentation using combined shape-intensity prior models, *International Journal of Computer Assisted Radiology and Surgery* 1 (2007) 341–350.
- [28] X. Huang, D. Metaxas, Metamorphs: Deformable shape and appearance models, *IEEE transactions on pattern analysis and machine intelligence* 30 (2008) 1444–59.
- [29] J. Yang, J. Duncan, 3d image segmentation of deformable objects with joint shape-intensity prior models using level sets, *Medical image analysis* 8 (2004) 285–94. doi:[10.1016/j.media.2004.06.008](https://doi.org/10.1016/j.media.2004.06.008).
- [30] T. Brox, J. Malik, Object segmentation by long term analysis of point trajectories, in: K. Daniilidis, P. Maragos, N. Paragios (Eds.), *Computer Vision – ECCV 2010*, Springer Berlin Heidelberg, Berlin, Heidelberg, 2010, pp. 282–295.
- [31] T. F. Cootes, G. J. Edwards, C. J. Taylor, Active appearance models, *IEEE Trans. Pattern Anal. Mach. Intell.* 23 (6) (2001) 681–685.
- [32] T. Chan, L. Vese, An active contour model without edges, in: *International Conference on Scale-Space Theories in Computer Vision*, 1999, pp. 141–151.